

PAPER

## Atomic-scale defects and electronic properties of a transferred synthesized MoS<sub>2</sub> monolayer

To cite this article: Ida Dela Marion *et al* 2018 *Nanotechnology* **29** 305703

View the [article online](#) for updates and enhancements.

### Related content

- [Theoretical characterisation of point defects on a MoS<sub>2</sub> monolayer by scanning tunnelling microscopy](#)  
C González, B Biel and Y J Dappe
- [2D Materials Advances: From Large Scale Synthesis and Controlled Heterostructures to Improved Characterization Techniques, Defects and Applications](#)  
Zhong Lin, Amber McCreary, Natalie Briggs *et al*.
- [One dimensional metallic edges in atomically thin WSe<sub>2</sub> induced by air exposure](#)  
Rafik Addou, Christopher M Smyth, Ji-Young Noh *et al*.










**IOP | ebooks™**

Bringing you innovative digital publishing with leading voices to create your essential collection of books in STEM research.

Start exploring the collection - download the first chapter of every title for free.

# Atomic-scale defects and electronic properties of a transferred synthesized MoS<sub>2</sub> monolayer

Ida Delač Marion<sup>1,6</sup> , Davor Čapeta<sup>1</sup>, Borna Pelić<sup>1</sup>, Fabio Faraguna<sup>2</sup> , Aurelio Gallardo<sup>3</sup> , Pablo Pou<sup>4</sup> , Blanca Biel<sup>5</sup> , Nataša Vujičić<sup>1</sup>  and Marko Kralj<sup>1,6</sup> 

<sup>1</sup> Center of Excellence for Advanced Materials and Sensing Devices, Institute of Physics, Bijenička 46, 10000 Zagreb, Croatia

<sup>2</sup> University of Zagreb, Faculty of Chemical Engineering and Technology, Marulićev trg 19, 10000 Zagreb, Croatia

<sup>3</sup> Institute of Physics of the Czech Academy of Sciences, v.v.i., Cukrovarnická 10, 162 00 Prague, Czechia

<sup>4</sup> Departamento de Física Teórica de la Materia Condensada & IFIMAC Facultad de Ciencias, Universidad Autónoma de Madrid, 28049 Madrid, Spain

<sup>5</sup> Department of Atomic, Molecular and Nuclear Physics, Faculty of Science, CITIC, & IBS, Granada, Universidad de Granada, 18071 Granada, Spain

E-mail: [idelac@ifs.hr](mailto:idelac@ifs.hr) and [mkralj@ifs.hr](mailto:mkralj@ifs.hr)

Received 28 February 2018, revised 20 April 2018

Accepted for publication 4 May 2018

Published 22 May 2018



CrossMark

## Abstract

MoS<sub>2</sub> monolayer samples were synthesized on a SiO<sub>2</sub>/Si wafer and transferred to Ir(111) for nano-scale characterization. The samples were extensively characterized during every step of the transfer process, and MoS<sub>2</sub> on the final substrate was examined down to the atomic level by scanning tunneling microscopy (STM). The procedures conducted yielded high-quality monolayer MoS<sub>2</sub> of millimeter-scale size with an average defect density of  $2 \times 10^{13} \text{ cm}^{-2}$ . The lift-off from the growth substrate was followed by a release of the tensile strain, visible in a widening of the optical band gap measured by photoluminescence. Subsequent transfer to the Ir(111) surface led to a strong drop of this optical signal but without further shifts of characteristic peaks. The electronic band gap was measured by scanning tunneling spectroscopy (STS), revealing n-doping and lateral nano-scale variations. The combined use of STM imaging and density functional theory (DFT) calculations allows us to identify the most recurring point-like defects as S vacancies.

Supplementary material for this article is available [online](#)

Keywords: MoS<sub>2</sub> monolayer, Ir(111), atomic defects, scanning tunneling microscopy (STM), scanning tunneling spectroscopy (STS), density functional theory (DFT), photoluminescence (PL)

(Some figures may appear in colour only in the online journal)

## Introduction

The present focus on semiconducting two-dimensional (2D) transition-metal dichalcogenide (TMD) materials in terms of atomic scale (point) defects, with MoS<sub>2</sub> being the most prominent member of the family, is widely debated in terms of

doping and modification of its band gap size and even the possible tuning of its direct/indirect semiconducting character [1–9]. As in the case of graphene, defects can limit the charge carrier performance in devices [10]. However, point defects in TMDs provide exciting possibilities for new developments in quantum optics and photonic technologies, as individual defects can serve as localization sites for excitons, thus serving as single photon emitters [11]. The structure of a TMD

<sup>6</sup> Authors to whom any correspondence should be addressed.

monolayer is more complex than that of graphene due to its sandwiched planar structure and its polymorphic character. Correspondingly, the appearance of atomic scale defects in TMDs compared to graphene relates to a richer phase-diagram of various defect types [12, 13]. Another important aspect of point defects, line defects, grain boundaries or edges, is their chemical functionality [14], which in the case of MoS<sub>2</sub> can be very useful in e.g. the hydrodesulfurization process. In any case, in order to obtain the desirable properties for electronic, optoelectronic or catalytic applications of TMD materials, relevant questions related to the characterization of the atomic scale defect types and their distributions (i.e. concentrations) must be addressed.

A viable source of material for large-scale applications is chemical synthesis, notably chemical vapor deposition (CVD) growth [15, 16]. Several studies report on a variation of quality of CVD samples, with a most prominent effect on their charge carrier mobility, with reported values scattered over an order of magnitude, from  $\sim 1$  to  $\sim 100$  of  $\text{cm}^2\text{V}^{-1}\text{s}^{-1}$ . While top-down device fabrication can clearly introduce a certain level of variation [17], the intrinsic quality of the material is the fundamental limiting parameter regarding electronic device performance [18], most critically in the case of the optical performance of MoS<sub>2</sub>-based devices, directly linked to morphology and defect structures within the single layers [19, 20].

Analogous to graphene, where the samples of highest quality are obtained by exfoliation from bulk [21], mechanically exfoliated single layers of TMDs from bulk crystals are generally considered to be of superior quality to CVD samples, because controlling sample homogeneity and atomic scale quality is challenging in CVD synthesis [22]. However, studies conducted on bulk exfoliated layers so far also indicate a significant presence of naturally occurring defects, which can severely affect the electronic properties of the sample and have been pointed out to be responsible for the variation of p- and/or n-doping in MoS<sub>2</sub> devices at the nano and micro scales [23]. The recent work of Vancso *et al* [24] presents an effort to set a limit to the concentration of atomic scale defects in MoS<sub>2</sub> as a benchmark for possible device performance. Mechanically exfoliated single layers from high structural quality bulk samples were studied, leading to an estimate of the lower limit for defect concentration. The surprising result in the STM characterization was the relatively high intrinsic concentration of sulfur mono-vacancies present in these native samples.

Our focus was on a transferred MoS<sub>2</sub> monolayer grown on a SiO<sub>2</sub>/Si substrate to: (i) a single-crystal Ir(111) surface or (ii) clean SiO<sub>2</sub>/Si substrates. While the latter route can be considered as an initial step to prepare quality devices from individual CVD monolayers or stacked heterostructures, the former enabled the characterization of atomic scale defects and local electronic properties with STM and STS; methods that require a conductive substrate. Unlike transmission electron microscopy (TEM) imaging, which enables the characterization of point defects in 2D materials, but at the same time causes the *in situ* activation and introduction of atomic scale defects [12, 25–27], STM characterization

presents a non-destructive route for atomic scale characterization of 2D samples. Thus, using the same transfer method to different substrates enables us to study transferred CVD-grown MoS<sub>2</sub> monolayers with techniques that are dependent on the substrates' characteristics. Furthermore, by combining these experimental findings with DFT modeling the influence of the substrate on the properties of the monolayers can be explored in more detail.

## Methods

An Ir(111) single crystal in a hat-shape form with diameters of 6–8 mm, orientation accuracy better than 0.1° and purity of 99.99% was obtained from Mateck GmbH, Germany. Its surface was cleaned in an ultra-high vacuum (UHV) chamber with a base pressure of  $10^{-9}$  mbar using previously established Ar<sup>+</sup> sputtering-O<sub>2</sub> annealing cycles described elsewhere [28], which ensure a clean surface of high structural quality consisting of large (cca 100 nm) terraces separated by monoatomic steps. The quality of the surface was confirmed with LEED and STM before taking the crystal out of the UHV chamber. The load lock mechanism mounted on the chamber enables relatively fast insertion and extraction of the samples without loss of UHV conditions in the chamber.

MoS<sub>2</sub> was grown in a homemade CVD system using aerosol assisted CVD. The MoO<sub>3</sub> precursor was aerosolized in 100 SCCM ultrapure argon using a 0.5 W 450 nm laser diode for local heating. Sulfur vapor was produced by heating 50–100 mg of S to 140 °C by a separate heater. The growth substrate, 285 nm SiO<sub>2</sub> on highly doped Si, was placed in the center of the furnace and heated to 750 °C during growth. After growth, the substrate was cooled in the furnace to 200 °C in an Ar stream before removal. Ir(111) was taken out of the UHV chamber via the load lock mechanism, and MoS<sub>2</sub> was transferred to Ir(111) using commercial polydimethylsiloxane (PDMS) film (X0 Gel-Film from GelPak) [29]. Briefly, a wafer with grown MoS<sub>2</sub> was covered with the PDMS film and floated on deionized water [30, 31]. The penetration of the water between the MoS<sub>2</sub> and SiO<sub>2</sub> caused delamination of the support film and MoS<sub>2</sub> in a few minutes. The released PDMS film was lifted with tweezers and, after drying, put in contact with the Ir(111) single crystal. The transfer process was completed by slowly lifting the PDMS film using a micromanipulator. After the transfer, the sample was immediately returned to the load lock, with the whole procedure being completed within 30 min from taking it out. The sample was annealed at 400 K (125 °C) for  $\approx 12$  h in UHV before STM imaging.

STM and STS measurements were performed using the Specs Aarhus VT-STM setup housed in a UHV chamber with a base pressure in the range of  $10^{-9}$  mbar. During measurements the sample was held at room temperature, with the bias voltage applied to it, while the STM tip was grounded. In order to obtain the STS spectra that have a dominant contribution from the sample, values of  $I_t$  were reduced, while  $V_b$  increased before the feedback-loop opening for spectroscopy in order to increase the tip-sample distance and

maximize the sample contribution in the spectroscopy [32]. The STM data was processed using WSxM [33] and Gwyddion [34] software. LEED measurements were performed at room temperature with an Omicron LEED system and the image from the screen was recorded with a Logitech C920 HD web camera.

SEM measurements were conducted using a VEGA 3 TESCAN microscope, with a detector of secondary electrons (energies 5–10 kV). AFM measurements were carried out with a Nanosurf FlexAFM in a dynamic force mode under ambient conditions. AppNano silicon tips with a nominal spring constant of 36–90 N m<sup>-1</sup>, a tip radius less than 10 nm and a nominal resonant frequency of 160–225 kHz were used. Images were processed with Gwyddion software [34].

An optical setup based on a confocal microscope in a backscattered configuration served for photoluminescence and Raman spectra measurements. A semiconductor laser with 532 nm (2.33 eV) excitation wavelength was focused to a spot size with a diameter of less than 2 μm on the sample by an objective lens (×50; N.A. = 0.75). Typical integration times were 20 s for PL and 60 s for Raman measurements and excitation power of the order of 500 μW was used to avoid heating effects [35]. The collected backscattered light was guided to a spectrometer equipped with two gratings (300 and 1800 lines/mm) and thermoelectrically cooled CCD was utilized for the measurements. Bearing in mind the spectrometer focal length, laser wavelength and grating specifications, a spectral resolution of about 0.8 meV for 300 lines/mm grating and 1.2 cm<sup>-1</sup> for 1800 lines/mm grating used for PL and Raman spectra collection, respectively, is obtained [36].

Density functional theory (DFT) calculations were performed using the Vienna *Ab initio* Simulation Package (VASP) [37, 38] under the general gradient approximation (GGA) with the Perdew–Burke–Ernzerhof (PBE) parametrization [39] to describe the exchange–correlation potential. VASP is a DFT-plane wave code that uses the pseudopotential approximation following the projector augmented wave (PAW) approach [40]. To include the van der Waals interactions in the exchange–correlation potential [41], the optB86b-vdW was employed during the simulations [42]. The energy cutoff was set to 450 eV and the tolerance for ionic and electronic convergence to 0.01 eV/Å and 10<sup>-5</sup> eV, respectively. For the density of states (DOS) calculations a smearing of 0.075 eV (SIGMA parameter) was set. The Ir(111) surface was simulated by a four layer slab, with only the two lower layers of the Ir slab kept fixed during the relaxation process. To study the relative stability of the MoS<sub>2</sub> monolayer over the Ir substrate three different positions were investigated, with either the Mo atom, the S atom or the center of the hollow of the MoS<sub>2</sub> monolayer lying directly over the Ir atoms of the topmost layer of the metal slab. The configuration where the Mo atoms lie directly over the Ir topmost atoms was the most stable one by 0.5 eV and was hence chosen as the initial geometry for our subsequent calculations. To minimize the strain due to the lattice mismatch between the MoS<sub>2</sub> and the Ir, a 3 × 3 MoS<sub>2</sub> supercell over a 30° rotated 2√3 × 2√3 Ir supercell was employed, doubling the

cell for the study of the defective structures. This results in a tensile strain of 0.37% that was imposed solely on the metal. The optimized lattice constant and band gap value for the pristine, freestanding MoS<sub>2</sub> monolayer are 3.164 Å and 1.74 eV, respectively, in very good agreement with previous theoretical [43–47] reports. As for the Ir surface, we found a lattice constant of 2.73 Å, also in good agreement with previous experimental [48] and DFT-based [49–51] results.

The STM images were simulated from the VASP-converged results by means of the WSxM software [33], within the Tersoff–Hamann approximation [52]. The impact of several point-like defects in a MoS<sub>2</sub> monolayer deposited on a Ir(111) substrate was studied by using a 6 × 6 supercell. The discretization of the first Brillouin zone was done by means of the Monkhorst–Pack scheme, using a grid of 5 × 5 × 1 special k-points for the relaxations and of 13 × 13 × 1 for the analysis of the electronic structure in the case of the 3 × 3 supercell, and a 3 × 3 × 1 scheme for relaxation and 7 × 7 × 1 for the 6 × 6 supercell. A vacuum layer of 20 Å in the perpendicular direction of the slab was employed to avoid interaction between the neighboring supercells.

## Results and discussion

### *Macroscopic quality and optical properties of the MoS<sub>2</sub> monolayer*

A MoS<sub>2</sub> monolayer was grown on 300 nm SiO<sub>2</sub>/Si substrates by CVD synthesis according to the procedures described in the methods section. The parameters for the synthesis of samples investigated in this work were adapted to ensure homogeneous monolayer growth over a large scale of millimeters without a significant amount of bilayers or multilayers. Nevertheless, the samples exhibited a small level of inhomogeneity, i.e. on substrate corners individual flakes with irregular (saw-like) edges could be found, as a consequence of the anisotropic growth conditions. The as-grown samples were inspected with optical microscopy (figure 1(a)), SEM (figures 1(b) and (c)) and AFM (see supplementary figure S1 available online at [stacks.iop.org/NANO/29/305703/mmedia](https://stacks.iop.org/NANO/29/305703/mmedia)). SEM and AFM imaging show the same features: uncoalesced flakes exhibit irregular edges, with occasional 5–10 nm tall wrinkles across the flakes (on length scales of several to hundreds of micrometers) and some scarce adsorbates, mostly on the edges of the flakes.

We have applied a transfer procedure using a PDMS stamp, a method which has already been successfully applied for the transfer of atomically thin layers between a wide range of different substrates [29–31]. The MoS<sub>2</sub> layer was systematically examined during every step of the transfer process with AFM, SEM, optical microscopy and PL and Raman spectroscopy. This enabled reliable control of the macroscopic and microscopic quality of the samples during the transfer process. Imaging at larger scales with an optical microscope or SEM (see figure 1(d)) confirms the uniform transfer of a large-area monolayer to both substrates. Although the monolayer area extends over millimeter distances, the crystallographic orientation of the MoS<sub>2</sub> randomly

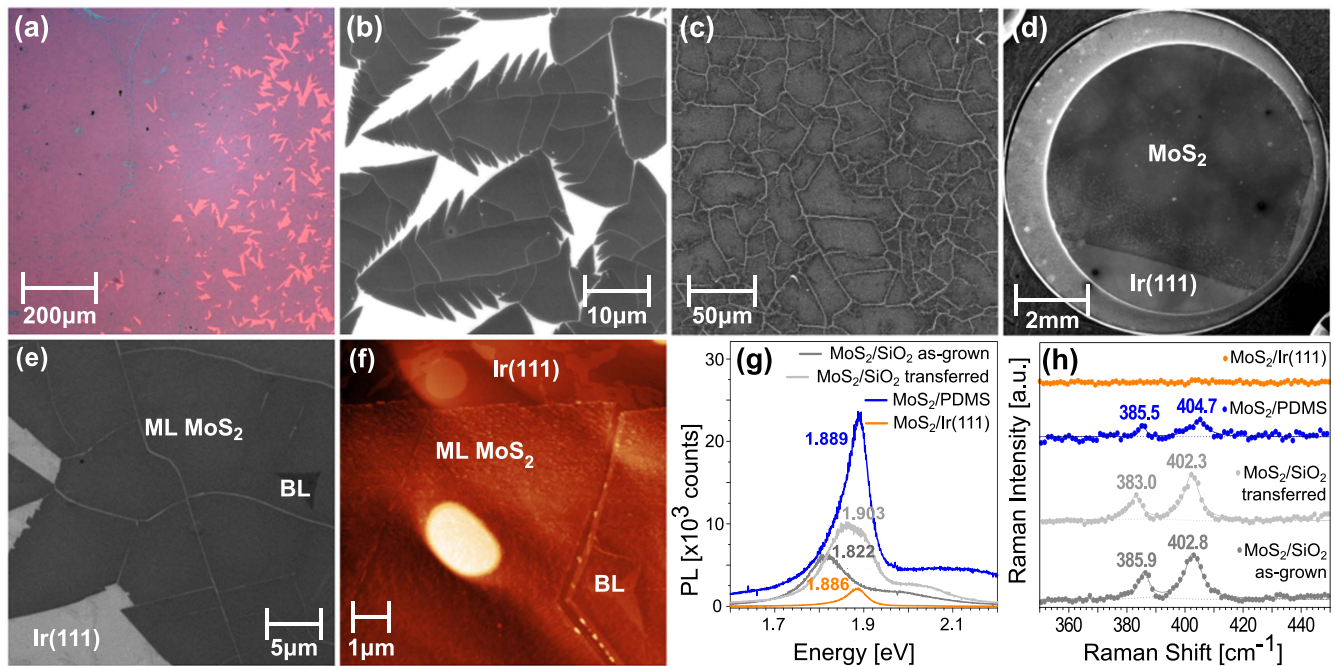


**Figure 1.** (a) As-grown MoS<sub>2</sub> monolayer on SiO<sub>2</sub>/Si substrate imaged with an optical microscope near the corner of the substrate. (b) SEM image of the area near the edge of the sample, with barely coalescing flakes with an irregular saw-like edge appearance. (c) Typical SEM image of an as-grown MoS<sub>2</sub> monolayer on the SiO<sub>2</sub>/Si substrate. (d) SEM overview image of the entire Ir(111) sample surface area covered dominantly by the transferred MoS<sub>2</sub> monolayer. (e) Characteristic SEM image of a homogeneous area of the MoS<sub>2</sub> monolayer transferred to Ir(111). (f) Typical AFM topography image of a MoS<sub>2</sub> monolayer on Ir(111). (g) PL and (h) Raman spectroscopy measurements of the MoS<sub>2</sub> monolayer on different substrates, as indicated. The energies in (g) correspond to the A exciton transition, while in (h) energies correspond to two characteristic Raman peaks: E<sub>2g</sub> mode (around 385 cm<sup>-1</sup>) and A<sub>1g</sub> mode (around 403 cm<sup>-1</sup>).

varies across the sample, due to the heterogeneous nucleation and the growth of randomly oriented single-crystal flakes on the amorphous SiO<sub>2</sub> substrate. This was confirmed with low energy electron diffraction (LEED), which shows a circular intensity from all possible rotations of MoS<sub>2</sub> on Ir(111) (shown in figure S2(a) in the supplementary material). A zoomed-in view to the micrometer scales with SEM and AFM (figures 1(e) and 1(f), respectively) show almost complete transfer, with small uncovered areas and/or negligible amount of bilayers. At the micrometer scale, the layer shows the presence of wrinkles or cracks every several micrometers, an effect known to be related to the local strain imposed by the growth at elevated temperatures or by subsequent mechanical manipulation. The samples indicated high uniformity at the nanometer scale and proved suitable for characterization with STM.

The PL spectra, presented in figure 1(g) consist of the A (1.82–1.90 eV) and B exciton (1.96–2.03 eV) peaks, that arise as a result of direct optical transitions from the near band edge [35, 53]. Moreover, there is another common feature at energies between 1.80 and 1.85 eV, associated with the emission from charged A excitons (trions, A<sup>-</sup>) [54]. In order to emphasize the influence of different substrates on the PL spectrum [55, 56], we show in figure 1(g) the energies corresponding to the A exciton transition. The extraction of detailed quantitative information from the fitted spectra is presented in the supplementary material, figure S3. The as-grown MoS<sub>2</sub> exhibits an optical band gap of 1.82 eV and immediately upon transfer (on all three explored substrates

SiO<sub>2</sub>, PDMS and Ir(111)) the optical band gap is blueshifted to 1.9 eV. This effect is attributed to the release of the tensile strain imposed by the CVD growth on SiO<sub>2</sub> due to the difference in the thermal expansion coefficient between MoS<sub>2</sub> and the silica substrate, which results in a significant difference in contraction during the cooling process from growth to room temperature [57]. Such strain is induced through interactions with the SiO<sub>2</sub> substrate and can be released after transferring MoS<sub>2</sub> to other substrates. The strain-related variation of the PL peak energy was obtained by DFT calculations [57] to be 44 meV per % strain, in good agreement to the experimental quantification for uniaxial strain [58, 59]. The values we measure correspond to biaxial strain, which was also recently analyzed for several different TMD single layers, including MoS<sub>2</sub> [60]. In our experiment, the A exciton peak shifts for about 80 meV, which corresponds to 1.57% of the global tensile strain release in the as-grown MoS<sub>2</sub> sample. Similar results were obtained by other groups [35, 57].

Generally, interaction of the layered material with the substrate influences its optical response, both in spectral shapes and positions. Bearing in mind the spectral linewidths, inhomogeneous broadening effects from extrinsic, substrate-related factors result in an overall broadening of the A exciton emission line on as-grown samples. Upon the lift-off process from the as-grown substrate and transfer to other substrates interaction with fresh substrates narrows the exciton emission lines to some typical values of about 40–50 meV [61]. This indicates that the monolayer–substrate interaction during the

CVD process is accompanied with extrinsic effects that significantly influence PL spectra [62, 63]. However, transfer to fresh SiO<sub>2</sub> is triggered by the n-doping induced by the substrate-borne moisture [56], which introduces a trion-related emission featuring broader peaks and longer wavelengths. [54, 64, 65]. On other substrates (PDMS, Ir(111)), the trion emission is less pronounced. The as-grown MoS<sub>2</sub>, which was not affected by the trapped moisture due to the high growth temperature, is also known to be intrinsically n-doped [56, 66], although the doping effect by the substrate is weaker than that of the substrate-borne moisture for those transferred. Thus, the trion population in transferred MoS<sub>2</sub>/SiO<sub>2</sub> is more pronounced compared to that of the as-grown sample, resulting in a more complex and asymmetric PL signal.

The overall PL signal intensity for transferred MoS<sub>2</sub>/SiO<sub>2</sub> is 64% greater than the PL intensity of the as-grown MoS<sub>2</sub>/SiO<sub>2</sub>. The photoluminescence signal of MoS<sub>2</sub> on PDMS shows practically no difference in peak position and overall higher PL intensity compared to that of MoS<sub>2</sub> on SiO<sub>2</sub> (both as-grown and transferred), due to the low interaction between the MoS<sub>2</sub> and the PDMS substrate [67]. Indeed, it has been shown that the optical properties of MoS<sub>2</sub> on PDMS strongly resemble those of the freestanding MoS<sub>2</sub> because of the reduced charge transfer between the PDMS and MoS<sub>2</sub>, which is much smaller than that of the MoS<sub>2</sub>/SiO<sub>2</sub> samples [55]. The PL intensity for the MoS<sub>2</sub> sample transferred on PDMS has a 3.9 times higher intensity than the as-grown MoS<sub>2</sub>/SiO<sub>2</sub> sample for the same excitation parameters. However, the metallic iridium substrate significantly lowers the PL intensity via the introduction of additional nonradiative paths for exciton recombination (such as charge transfer processes and dipole–dipole interaction) [55, 68–71], and the absolute observed PL intensity on Ir is 2.8 times lower than on SiO<sub>2</sub> for the same incident laser power.

Raman spectroscopy has proven to be an effective tool to determine not only the number of layers of MoS<sub>2</sub>, but also the built-in strain [72] in the layers as well as their doping level [73]. Figure 1(h) shows a comparison of the Raman spectra measured for MoS<sub>2</sub> single layers deposited onto the different substrates. In the Raman spectrum, two characteristic Raman peaks appear: the  $E_{2g}^1$  mode (around 385 cm<sup>-1</sup>) and  $A_{1g}$  mode (around 403 cm<sup>-1</sup>). The distance between the  $A_{1g}$  and  $E_{2g}^1$  peaks ( $\Delta = A_{1g} - E_{2g}^1$ ) was approximately 18.5 cm<sup>-1</sup>, which is characteristic for monolayer MoS<sub>2</sub>. The intensities and energies of the  $E_{2g}^1$  and  $A_{1g}$  modes are clearly modulated by the substrate. The Raman spectrum on a specific sample was collected at the same location where the corresponding PL spectrum was taken. Softening of the  $E_{2g}^1$  mode is observed after the transfer processes, in accordance with the known sensitivity to strain in this material [72, 74]. Rice *et al* [72] measured a shift of the  $E_{2g}^1$  mode of 2.1 cm<sup>-1</sup> per % of uniaxial strain, while Hui *et al* [74] found a shift of 4.7 cm<sup>-1</sup> per % of biaxial strain. Bearing in mind our global strain release after the transfer to the fresh SiO<sub>2</sub> substrate, a redshift of the  $E_{2g}^1$  mode frequency by 2.9 cm<sup>-1</sup> is thus expected in accordance to previous studies [72, 74]. However, the  $A_{1g}$  mode exhibits a sizeable softening with doping [55, 56, 73], which further supports the n-doping scenario of the sample induced by transfer to different substrates, which was also

subsequently confirmed with STS for MoS<sub>2</sub>/Ir(111) (as elaborated in the following). The redshift of the  $A_{1g}$  peak for monolayer MoS<sub>2</sub> on SiO<sub>2</sub> substrates compared to the MoS<sub>2</sub>/PDMS sample indicates an increased concentration of electrons, both intrinsically and due to the n-doping by the substrate-borne moisture during the transfer. The complete absence of the Raman signal on the iridium substrate at our experimental conditions can be explained by the fact that iridium as a substrate suppresses the active Raman modes [75]. Both Ir(111) [76] and Pd(111) [77, 78] are intermediately between strongly and weakly interacting metal substrates for 2D materials, where the strength of the film–substrate interaction correlates with the ability to observe the Raman-active phonons.

#### *Microscopic structure and electronic properties of the MoS<sub>2</sub> monolayer*

For the STM characterization, samples transferred from the growth substrate to Ir(111) were readily inserted into a load lock system of an ultra-high vacuum (UHV) setup and quickly pumped down and baked at 400 K for 10–12 h before insertion into UHV, although the STM imaging was performed at room temperature. Even though the substrate's exposure time to ambient conditions was short, there is a possibility that during the transfer process a small amount of adsorbates, e.g. water molecules, became trapped in between the 2D overlayer and the substrate. In the UHV system, samples were preliminarily inspected by LEED (see above and in the supplementary material in figure S2(a)) and extensively characterized with STM and STS. In specific cases, when STM imaging included an area of MoS<sub>2</sub> flake edges, a dynamical ripping or flipping of the flake edges often occurred (see figure S2(b) in the supplementary material). This indicates a relatively weak bonding strength of the MoS<sub>2</sub> overlayer to the metal substrate. In areas away from the MoS<sub>2</sub> edges, STM imaging was very stable in the whole range of imaging parameters used. A set of large-scale STM topographs is presented in figure 2. The characteristic feature is clearly visible over all the scan ranges in figures 2(a)–(c) with regard to a corrugation whose amplitude varies between 0.2 nm and 2 nm at characteristic lateral scales of 5–10 nm. Specifically, the height variation in figure 2(c) is 0.5 nm.

The rippling of the 2D layer evokes some similarities to the well-known moiré effect typical for epitaxial systems, such as, for example, graphene on Ir(111) [79–82]. The distinction between the periodic moiré structure of epitaxial graphene and a nonperiodic long-range corrugation of the MoS<sub>2</sub> overlayer is, however, pronounced, and the nano-scale rippling of the MoS<sub>2</sub> overlayer can be more directly compared to the topography of single-layer graphene on a SiO<sub>2</sub>/Si surface [83, 84], which can only be partly attributed to the native corrugations of the substrate. Specifically, the high measured corrugation suggests that the sample could be considered as quasi-freestanding at some elevated areas while in close connection to the metal substrate at others. This is supported by the STS measurements presented below, which show a gap close to the one of freestanding MoS<sub>2</sub>. The interaction with the Ir(111), while not strong enough

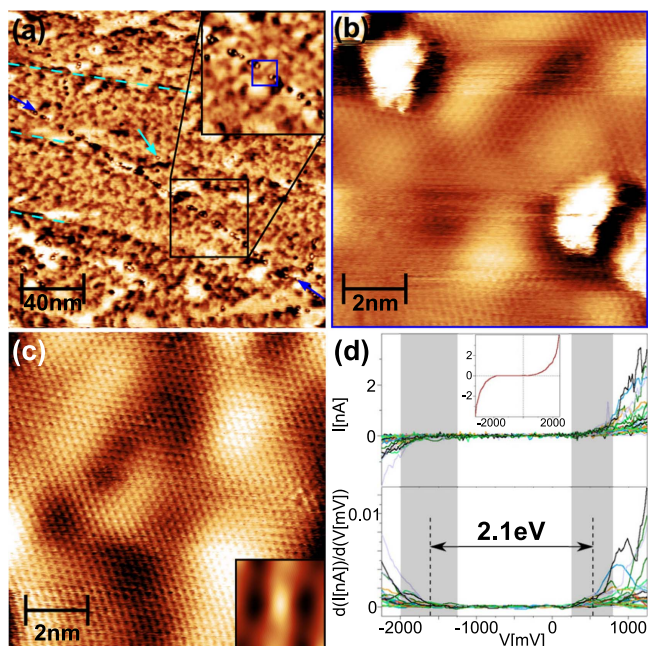


**Figure 2.** (a) Large-scale STM image of the MoS<sub>2</sub> monolayer on Ir(111) with the Ir steps visible underneath indicated with dashed pale blue lines, line of point defects (dark blue arrows) and single point defects (pale blue arrow). (b) A zoomed-in view between the point defects is shown in the inset of (a). (c) Typical atomic scale STM image of the corrugations, with an autocorrelation image shown in the inset. (d) Top:  $I(V)$  spectra measured with STS, with one typical spectrum in the inset. Bottom:  $dI/dV$  spectra calculated from the measured  $I(V)$  spectra. The gray bars show the dispersion of the gap edges found for the different spectra, while the averaged width of all the curves is represented with a black arrow.

to induce the flattening of the corrugated monolayer, is nevertheless a possible source of n-doping as confirmed by previous works [50, 51]. The origin of the corrugations in our samples can thus be ascribed to the laterally-varying interaction with the substrate (as visible from atomic contrast changes in STM imaging), keeping in mind the general notion that the MoS<sub>2</sub>-Ir(111) interaction appears to be relatively weak, as evidenced from the previously mentioned occasional ripping of the flake edges during imaging. Recently, similar corrugations were observed on epitaxial MoS<sub>2</sub> on graphene [85], which also exhibits a similar band gap size and position as those measured in our sample. Finally, as pointed out earlier, in our case we cannot exclude the possibility that the rippling effect is triggered by randomly trapped and/or intercalated atoms or molecules between the MoS<sub>2</sub> and Ir(111) substrate that might have been introduced during the transfer process.

Additional visible features in figures 2(a)–(c) include the clear presence of Ir(111) substrate atomic steps below a continuous MoS<sub>2</sub> layer (light blue dashed lines in figure 2(a)) or larger adsorbate-like defects [86] visible even at the largest scales and imaged as bright protrusions with a locally extended dark surrounding (figure 2(a) and its inset, shown in more detail in figure 2(b)). From our characterization it appears that these types of defects are sometimes formed along straight lines in a direction not necessarily correlated to that of the Ir steps, indicating that they are intrinsically related

to MoS<sub>2</sub>. Zooming-in on such lines of larger defects does not reveal an apparent grain boundary, instead atomic resolution shows a continuous propagation of the crystal lattice across the line separating individual adjacent protrusions (see figure 2(b)). We cannot, however, exclude the possibility of grain boundaries with very small lattice rotations, as often observed in graphene [87], where small lattice rotations can be noticed from the rotation of the moiré lattice, which acts as a magnifying lens. In the absence of such a magnifying lens, we can only argue that as long as the bright protrusions follow the grain boundary the lattice rotation angle is within the range of  $\sim 1^\circ$ , i.e. extremely low.

Regarding the atomic resolution imaging of the MoS<sub>2</sub> lattice without defects, we note that the lattice was imaged in two different contrast modulations—either a honeycomb or hexagonal lattice—each of which shows a different relative darkness of the Mo atoms and hollow sites with respect to the (always bright) S atoms. Similar varying lattice contrast effects are already known for graphene-based materials [88–90]. In our case, such brightness modulations might be related to a MoS<sub>2</sub>-metal distance variation or to a change in the interaction between the metal and the MoS<sub>2</sub>. Changes in the tip-MoS<sub>2</sub> distance could be responsible for the observed changes in the atomic contrast, as suggested by Altibelli *et al* [91]. In that work, even the Mo atoms were observed as bright protrusions for tip-sample distances close to the contact regime, as a result of the current saturation over the S atoms due to the electronic multiple scattering. In this distance regime, other effects such as the atomic and charge rearrangement would also have an impact on the electronic structure, hence modifying the atomic contrast. We must note that there is no systematic connection of the elevated (brighter) or lower (darker) areas to either type of contrast: as visible in figure 2(c) and in more detail in S2(c), darker areas on the top and bottom of the image exhibit a honeycomb lattice contrast, while the darker area in the middle of the image exhibits a hexagonal contrast, and the same is valid for the brighter areas. By using the well-known lattice parameter of epitaxial graphene on Ir(111) [79] and measurements on MoS<sub>2</sub> performed with the same tip, we determine the lattice parameter of our MoS<sub>2</sub> samples to be  $(0.30 \pm 0.01)$  nm, which is in accordance with previously reported values [92–94]. In addition, we also tested the stability of MoS<sub>2</sub> ML on Ir(111) to subsequent annealing (see figure S4 in the supplementary material), which significantly deteriorated their atomic scale quality.

In the course of the STM characterization in UHV, an electronic band gap of MoS<sub>2</sub> on Ir(111) was measured with  $I(V)$  STS at constant tip-sample separation. We note a certain limitation of this type of spectroscopy, which is dominated by contributions from the center of the Brillouin zone while contributions of states with higher parallel momentum are less pronounced. This notion has thus to be taken into account in the interpretation of the measured values, which is also the case of other literature values obtained by the same type of spectroscopy. STS measurements were typically performed after a detailed atomic resolution characterization was obtained, to guarantee that there were no adsorbates or large defects and/or domain boundaries within the area inspected by STS, where the several  $I(V)$  spectra were taken at different

parts of the image. The procedure was repeated for different areas of the sample, always within the area without large defects. Since our experiments were performed at room temperature and there is a certain level of thermal drift we were not able to make spectroscopy measurements of individual point defects. Measured spectra and their derivatives are showed in figure 2(d), confirming in each case the semi-conducting character and n-doping of the MoS<sub>2</sub> monolayer. The derivatives ( $dI/dV$  spectra) enabled us to make a reliable extraction of the gap width from the individual spectra. The determined average width of the band gap is found to be  $(2.1 \pm 0.1)$  eV. Furthermore, from the difference between the band gap obtained from STS and the optical band gap an exciton binding energy of 0.2 eV can be estimated, which is in accordance with previous reports [95–97].

We have performed DFT modeling of the freestanding MoS<sub>2</sub> and the aligned epitaxial MoS<sub>2</sub> on Ir(111). Details about the relaxation process can be found in the methods section. The two simulated systems present idealistic situations of MoS<sub>2</sub> (a) without any interaction with its surrounding, and (b) one in well-defined chemical contact with the metal substrate, which are not strictly realized in our experimental system because the alignment of the MoS<sub>2</sub> varies randomly across the surface, and because the MoS<sub>2</sub>–Ir separation changes across the sample, as found in STM topography characterization (see figure 2(c)). However, comparison of the DFT and experimental results greatly helped us in qualitative and quantitative understanding of the energy shift observed experimentally.

In the limit of the epitaxial model, DFT calculations show that the bonding with the substrate results in hybridization of the MoS<sub>2</sub> states with the metal, and triggers the appearance of the hybridized states in the MoS<sub>2</sub> gap, thus inducing the metallization of the MoS<sub>2</sub> monolayer [50, 51]. This is easily understood considering the calculated equilibrium distance is only 2.31 Å, indicating chemisorption of the MoS<sub>2</sub> on Ir(111). This effect is visible in figure 3, which depicts the local density of states (LDOS) of the Mo and S atoms of the MoS<sub>2</sub> on Ir(111) (solid lines in main panels of figures 3(a) and (b)) in comparison to their counterparts in the freestanding structure, displayed in the insets. The effect is stronger for the Mo atoms, due to their comparatively larger density of states, but can be also identified on the S states, especially on those at the bottom layer, whose overlapping with the metal states is larger. Additionally, the metal–MoS<sub>2</sub> interaction pins the Fermi level [50, 51] and induces a shift of the MoS<sub>2</sub> levels by  $-1$  eV towards negative energies. This effect can also be seen in figures 3(a) and (b) by direct comparison between the LDOS of the freestanding system, displayed in the insets, and the same LDOS curves (dashed lines in the main frames), which have been accordingly shifted and superimposed to the LDOS of the epitaxial system as a reference. The two peaks at  $-0.74$  eV and  $2.23$  eV in the Mo's LDOS of the freestanding case are clearly identifiable also in the Mo's LDOS of the epitaxial structure, albeit now located at  $-1.92$  eV and  $1.20$  eV, respectively. Similar features can be recognized, although less clearly, in the LDOS of the S atoms. The aforementioned peaks broaden in the presence of the metal, hence confirming the metal-induced hybridization of the states. In contrast to the ideal epitaxial system, as previously discussed, the high corrugation of the

mechanically transferred sample and the measured gap, comparable to that of the freestanding MoS<sub>2</sub>, confirm the local existence of quasi-freestanding zones over the substrate, in which the coupling to the metal, and hence the state hybridization leading to the gap closure, would be greatly diminished.

The simulated STM image of pristine, freestanding MoS<sub>2</sub> within the Tersoff–Haman (TH) approach [98] show, for energies outside the MoS<sub>2</sub> gap, the S atoms of the top layer as bright protrusions, then the hollow, and then darker, Mo atoms, (as depicted in the top panel of the figure 3(c)) in agreement with the experimental images in figure 2. This is also the case for the epitaxial system, as shown in the bottom panel of figure 3(c). The main difference is the modulation induced by the moiré pattern, clearly visible in the different contrast of the Mo atoms.

#### *Atomic defects in the MoS<sub>2</sub> monolayer*

In principle, STM imaging on smaller scales enables the visualization of atomic defects even before the crystal lattice is clearly resolved, as shown in figures 4(a) and S2(d). Such imaging also enables an insight into lateral variations of the local concentration of point defects. For example, the upper right area of figure 4(a) is much poorer in defects than that few tens of nanometers to the left, which shows a much higher concentration of defects. It is also apparent that the different concentration of defects is not specifically related to the seemingly higher or lower rippled areas of the MoS<sub>2</sub> layer, clearly visible in larger magnification images in figures 4(b) and (c). Defect density varies on the scale of tens of nanometers, with the maximum local defect density found in our samples around  $8 \times 10^{13}$  cm<sup>-2</sup>, while the average value extracted from the analysis of the obtained STM images is  $2 \times 10^{13}$  cm<sup>-2</sup>, which is in the same range as reported for the natural MoS<sub>2</sub> [24, 86]. Considering the fact that there are areas of the sample with considerably fewer defects than the average, we believe that further optimization of the synthesis parameters may lead to even higher quality of the CVD MoS<sub>2</sub> monolayer samples.

The visibility and appearance of the point defects in the STM images strongly depends on the applied imaging parameters (bias voltage and tunneling current), as expected from the semiconducting nature of MoS<sub>2</sub> and in line with previous reports [24, 86]. In contrast to the featureless larger bright protrusions mentioned in the description of figure 2, there are at least two types of atomic defects identified by STM. Both types are visible only within a small range of bias voltages. Moreover, their appearance changes within that narrow voltage range and we could resolve different shapes. Examples of similar looking shapes are indicated by circles or arrows in figures 4(b)–(e). For the additional STM images obtained with different imaging parameters, please see the supplementary material (figure S5). Some insight into the nature of these imaged atomic defects can be gained with the help of the DFT calculations presented below.

DFT calculations regarding the atomic defects were focused on four types of point-like defects, which according to the literature [12] and method of growth appear as the most probable ones induced during the growth process: an S vacancy



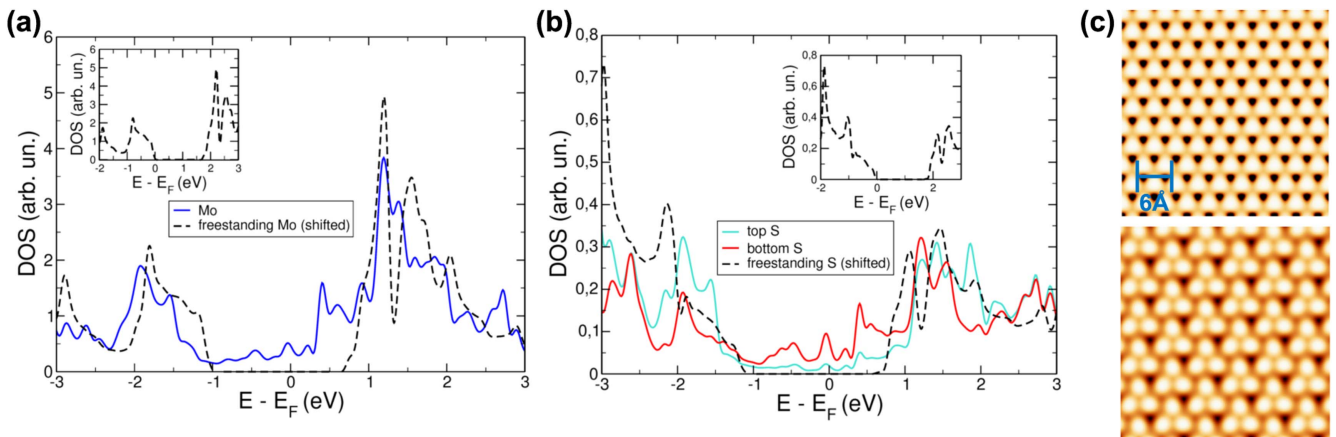


**Figure 3.** Local density of states (LDOS) of the Mo (a) and the S (b) atoms for both the epitaxial (solid lines) and the freestanding (dashed black line) MoS<sub>2</sub> monolayer. The insets show LDOS of the Mo (a) and S (b) atoms for the freestanding MoS<sub>2</sub> monolayer. For comparison, the LDOS of both the Mo and the S atoms in the freestanding monolayer is shifted by  $-1$  eV and superimposed to that of the epitaxial MoS<sub>2</sub> atoms in the main panels. The metal substrate induces a shift of  $\sim 1$  eV towards negative energies to the LDOS of the MoS<sub>2</sub> monolayer. (c) TH-STM simulated images for the pristine freestanding MoS<sub>2</sub> (top) and the epitaxial MoS<sub>2</sub>/Ir(111) system (bottom) at  $V = -0.1$  eV.

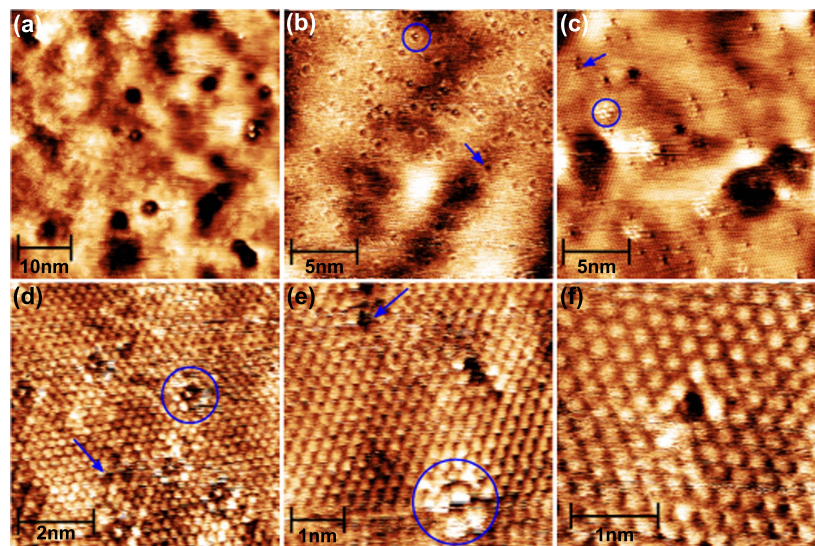


**Figure 4.** STM images of the atomic defects exhibiting dependence of their appearance on the imaging parameters. Generally, (up to) two types of defects can be distinguished, with similar looking defects in (b)–(d) indicated by arrows and circles. (a) Larger area with variations in defect density ( $V_b = 170$  mV and  $I_t = 1.2$  nA). (b)  $V_b = 260$  mV and  $I_t = 3$  nA, (c)  $V_b = -136$  mV and  $I_t = -1.4$  nA, (d)  $V_b = 51$  mV and  $I_t = 1.6$  nA. (e) Zoomed-in area around the indicated defects in (c) ( $V_b = -136$  mV and  $I_t = -1.4$  nA). (f) Zoomed-in view of a triangle-shaped point defect ( $V_b = -136$  mV and  $I_t = -1.8$  nA).

at the top layer of the MoS<sub>2</sub>, an S vacancy at the opposite side of the monolayer (i.e., closer to the metal substrate), a vertical S divacancy, and an S adatom at the MoS<sub>2</sub> top layer. Extensive analyses of the stability and the structural and electronic properties of these defects and their calculated STM images for the freestanding MoS<sub>2</sub> monolayer have been performed in previous works [2, 95, 99–102]. The main effect of the point-like defects containing S vacancies on the electronic structure of the freestanding MoS<sub>2</sub> is the introduction of several localized states in the LDOS midgap, associated to the dangling bonds created by the suppression of the S atoms (see figures S6 and S7 in the supplementary material). In the case of the S adatom this peak is pinned at the Fermi level at the top of the MoS<sub>2</sub> valence band, with no additional peaks appearing at the midgap.

The simulated TH-STM images at a bias voltage of  $-0.1$  V, corresponding to valence band states close to the Fermi energy, are displayed in the top panel of figure 5, and show the S vacancy at the top layer as a bright spot, which largely comes from the contribution to the LDOS of the neighboring Mo dangling bonds, surrounded by a narrow darker halo and, further away, by a very bright feature extending over 2–3 of the nearest neighbors. However, the dark halo surrounding the vacancy is spread over the neighboring atoms when the tip approaches the MoS<sub>2</sub> at the opposite side of the vacancy (or, equivalently, when the missing S atom is located at the bottom layer). The simulated STM images of the S divacancy present a strong resemblance to those of the S monovacancy in the top layer, rather than to

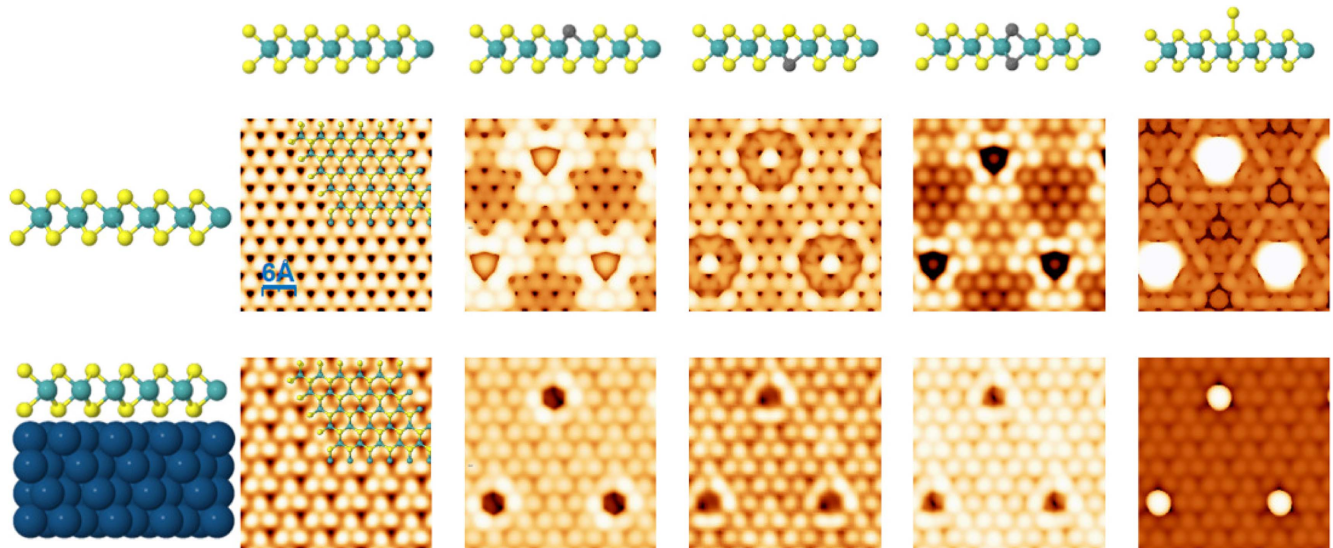


**Figure 5.** Simulated STM images for the freestanding (top panel) and the epitaxial (bottom panel) MoS<sub>2</sub> monolayer. From left to right: pristine structure, S vacancy at the top layer, S vacancy at the bottom layer, S divacancy, and S adatom. The ball-and-stick models on top of the figure showcase each type of defect. S atoms are shown in yellow, Mo atoms in cyan, Ir atoms in dark blue, and the gray atoms show the position of the missing S atoms. The images were taken at a bias voltage  $V = -0.1$  V and an isosurface value of  $2 \times 10^{-6}$  for the freestanding system and  $1 \times 10^{-6}$  for the epitaxial one.

the images of the S vacancy in the bottom layer, which might help to aid their discrimination when observed experimentally.

For all the S vacancies studied here, and for bias voltages at the defect level energy within the gap energy range, the contribution to the LDOS of the dangling bonds associated to the defect is the only one available in the midgap, and hence only the states associated to the dangling bonds left by the missing atoms can be seen, appearing as a bright spot in the TH image (not shown). As for the adatom, its strong contribution to the LDOS at energies close to the Fermi level, in addition to its higher location over the monolayer, is responsible for the broad, bright spot in the STM images, in clear contrast to the S vacancies' defects.

The n-doping induced by the metallic Ir(111) substrate dramatically modifies the LDOS of the defect states for the S vacancies, splitting the sharp, very localized peaks into several ones, and broadening them as a result of their hybridization with the metal states (as elaborated in more detail in figures S6 and S7 in the supplementary material). The defect states are indeed much more affected by the metal substrate than the states of atoms lying further apart from the defect site, which remain practically unaltered except for the shift towards negative energies mentioned previously. The defect states are located very close to the Fermi level for all three S vacancy cases. The adatom defect strongly differs again from the other three studied defects, and besides the energy shift induced by the n-doping and a minor broadening its appearance is remarkably similar to that of the freestanding case.

As seen in the TH-STM images in the top and bottom panels of figure 5, compared to the freestanding case, in the epitaxial system the point-like defects considered here have a much smaller effect on the surrounding atoms (up to  $\approx 5$  Å) at energies in the vicinity of the freestanding MoS<sub>2</sub> gap. This is more easily distinguished from the STM images, since the

LDOS of the surrounding S atoms and that of the next-neighbors Mo atoms exhibit only minimal variations. For the S vacancies, the simulated STM images in figures 5 and S8 in the supplementary material show, also at energies close to the defect energy, a dark, triangular-shaped hole where the defect should be, even for the case of the S vacancy at the bottom layer. The rationale behind this is that the metal-hybridized S states are still more easily accessible than the very localized defect state, increasing their visibility, and the lost contribution to the DOS from the missing S atom leads to a decrease in the current and hence to the dark spot right at the vacancy site. The STM image of the S divacancy retains its strong similarity to that of the single S vacancy at the top MoS<sub>2</sub> layer, making them barely distinguishable. Thus, we can confirm that the defects seen in the experiment as dark triangles correspond to point-like, missing S related defects, while the more complex-shaped ones could not be unambiguously identified. As for the S adatom, the metal considerably reduces the extension of the bright spot found for the freestanding case, but its STM image shows nevertheless the characteristic bright spot associated to the adatom states' contribution to the MoS<sub>2</sub> LDOS (figures 5 and S8).

## Conclusions

In this work we have established a reproducible transfer procedure of large-scale MoS<sub>2</sub> monolayer samples obtained by CVD synthesis onto a well-defined single-crystal metal substrate. In the course of this work we directly compared the spectroscopic and microscopic properties of CVD samples. The characterization of the transferred samples indicates high-quality millimeter-sized monolayers with a low defect density within the range of values reported for natural MoS<sub>2</sub>. We

have investigated the influence of the substrate regarding the electronic structure, doping and the exciton response by measuring optical properties (PL and Raman spectroscopy), STS and DFT simulations. Our samples exhibit n-type doping that can be attributed to the intrinsic presence of defects, the substrate-borne moisture introduced during the transfer process and/or the interaction with the metallic substrate. During the transfer process, immediately after lift-off from the substrate on which the layer was synthesized, release of the tensile strain occurs as evidenced from the widening of the optical band gap. Upon transfer to the Ir(111) surface there is a strong suppression of the PL signal due to interaction with the metallic substrate. From the difference of the electronic band gap measured by STS of 2.1 eV and the optical band gap from PL of 1.9 eV, an estimated exciton binding energy of  $\sim 0.2$  eV is obtained. A comparison of the experimental findings and simulations considering freestanding and epitaxial MoS<sub>2</sub> on Ir(111) suggests that the investigated samples on Ir(111) are quasi-freestanding or weakly coupled to the substrate, based on the observation of the semiconducting band gap, nano-scale rippling of flakes and weak binding of the flake edges. The observed height variations across the sample could be connected to topographic corrugation, interaction with the substrate or to the possibility of trapped/intercalated atoms between the monolayer and the Ir substrate introduced during the transfer process, in which case they could influence the MoS<sub>2</sub>-substrate interaction and hence the sample doping. The simulations of the defects explain the observation of two main types of defects in STM images, with the possibility of the S vacancy on the top layer and divacancy looking the same (as a dark triangle or circle). Also, since all three types of S vacancy defects give rise to non-dispersive states in the gap at similar energies, it is expected that they should be visible for the same imaging parameters.

## Acknowledgments

The authors gratefully acknowledge financial support from the European Regional Development Fund for the ‘Center of Excellence for Advanced Materials and Sensing Devices’ (Grant No. KK.01.1.1.01.0001) and support from the Croatian Science Foundation (Grant No. IP-2016-06-3211), the computational resources provided by the Spanish Supercomputing Network (RES) and University of Granada-CSIRC, as well as financial support from the TEC2014-59730-R and MAT2014-54484-P projects. Research by BB was supported by MINECO (Spain) under the Ramon y Cajal fellowship program (RYC-2012-10381).

## ORCID iDs

Ida Delač Marion  <https://orcid.org/0000-0002-7481-6542>  
 Fabio Faraguna  <https://orcid.org/0000-0003-4866-1038>  
 Aurelio Gallardo  <https://orcid.org/0000-0001-6544-7637>  
 Pablo Pou  <https://orcid.org/0000-0002-5854-8218>  
 Blanca Biel  <https://orcid.org/0000-0003-0574-1214>

Nataša Vujičić  <https://orcid.org/0000-0002-5437-5786>  
 Marko Kralj  <https://orcid.org/0000-0002-9786-3130>

## References

- [1] Mas-Ballesté R, Gómez-Navarro C, Gómez-Herrero J and Zamora F 2011 2D materials: to graphene and beyond *Nanoscale* **3** 20–30
- [2] Komsa H P and Krasheninnikov A V 2012 Effects of confinement and environment on the electronic structure and exciton binding energy of MoS<sub>2</sub> from first principles *Phys. Rev. B* **86** 241201(R)
- [3] Butler S Z *et al* 2013 Progress, challenges, and opportunities in two-dimensional materials beyond graphene *ACS Nano* **7** 2898–926
- [4] Xu M, Liang T, Shi M and Chen H 2013 Graphene-like two-dimensional materials *Chem. Rev.* **113** 3766–98
- [5] Fiori G, Bonaccorso F, Iannaccone G, Palacios T, Neumaier D, Seabaugh A, Banerjee S K and Colombo L 2014 Electronics based on two-dimensional materials *Nat. Nanotechnol.* **9** 768–79
- [6] Bhimanapati G R *et al* 2015 Recent advances in two-dimensional materials beyond graphene *ACS Nano* **9** 11509–39
- [7] Gupta A, Sakthivel T and Seal S 2015 Recent development in 2D materials beyond graphene *Prog. Mater. Sci.* **73** 44–126
- [8] Novoselov K S, Mishchenko A, Carvalho A and Neto A H C 2016 2D materials and van der Waals heterostructures *Science* **353** aac9439
- [9] Tan C *et al* 2017 Recent advances in ultrathin two-dimensional nanomaterials *Chem. Rev.* **117** 6225–331
- [10] Yu Z *et al* 2014 Towards intrinsic charge transport in monolayer molybdenum disulfide by defect and interface engineering *Nat. Commun.* **5** 5290
- [11] He Y-M *et al* 2015 Single quantum emitters in monolayer semiconductors *Nat. Nanotechnol.* **10** 497–502
- [12] Hong J *et al* 2015 Exploring atomic defects in molybdenum disulfide monolayers *Nat. Commun.* **6** 6293
- [13] Lin Z, Carvalho B R, Kahn E, Lv R, Rao R, Terrones H, Pimenta M A and Terrones M 2016 Defect engineering of two-dimensional transition metal dichalcogenides *2D Mater.* **3** 022002
- [14] Chhowalla M, Shin H S, Eda G, Li L-J, Loh K P and Zhang H 2013 Chemistry of two-dimensional layered transition metal dichalcogenide nanosheets *Nat. Chem.* **5** 263–75
- [15] Lee Y H *et al* 2012 Synthesis of large-area MoS<sub>2</sub> atomic layers with chemical vapor deposition *Adv. Mater. (Weinheim, Ger.)* **24** 2320–5
- [16] Chen W *et al* 2015 Oxygen-assisted chemical vapor deposition growth of large single-crystal and high-quality monolayer MoS<sub>2</sub> *J. Am. Chem. Soc.* **137** 15632–5
- [17] Allain A, Kang J, Banerjee K and Kis A 2015 Electrical contacts to two-dimensional semiconductors *Nat. Mater.* **14** 1195–205
- [18] Zhu W, Low T, Lee Y H, Wang H, Farmer D B, Kong J, Xia F and Avouris P 2014 Electronic transport and device prospects of monolayer molybdenum disulfide grown by chemical vapour deposition *Nat. Commun.* **5** 1–8
- [19] Nan H *et al* 2014 Strong photoluminescence enhancement of MoS<sub>2</sub> through defect engineering and oxygen bonding *ACS Nano* **8** 5738–45
- [20] Zhang G, Wang J, Wu Z, Shi R, Ouyang W, Amini A, Chandrashekar B N, Wang N and Cheng C 2017 Shape-dependent defect structures of monolayer strong photoluminescence enhancement of MoS<sub>2</sub> through defect engineering and oxygen bonding crystals grown by chemical vapor deposition *ACS Appl. Mater. Interfaces* **9** 763–70

- [21] Bolotin K, Sikes K, Jiang Z, Klima M, Fudenberg G, Hone J, Kim P and Stormer H 2008 Ultrahigh electron mobility in suspended graphene *Solid State Commun.* **146** 351–5
- [22] Lin Z *et al* 2016 2D materials advances: from large scale synthesis and controlled heterostructures to improved characterization techniques, defects and applications *2D Mater.* **3** 042001
- [23] McDonnell S, Addou R, Buie C, Wallace R M and Hinkle C L 2014 Defect-dominated doping and contact resistance in MoS<sub>2</sub> *ACS Nano* **8** 2880–8
- [24] Vancso P, Magda G Z, Peto J, Noh J Y, Kim Y S, Hwang C, Biro L P and Tapasztó L 2016 The intrinsic defect structure of exfoliated MoS<sub>2</sub> single layers revealed by scanning tunneling microscopy *Sci. Rep.* **6** 29726
- [25] Hashimoto A, Suenaga K, Gloter A, Urita K and Iijima S 2004 Direct evidence for atomic defects in graphene layers *Nature* **430** 870–3
- [26] Meyer J C, Kisielowski C, Erni R, Rossell M D, Crommie M F and Zettl A 2008 Direct imaging of lattice atoms and topological defects in graphene membranes *Nano Lett.* **8** 3582–6
- [27] Komsa H P, Kotakoski J, Kurasch S, Lehtinen O, Kaiser U and Krasheninnikov A V 2012 Two-dimensional transition metal dichalcogenides under electron irradiation: defect production and doping *Phys. Rev. Lett.* **109** 035503
- [28] Petrović M, Sadowski J T, Šiber A and Kralj M 2015 Wrinkles of graphene on Ir(111): macroscopic network ordering and internal multi-lobed structure *Carbon* **94** 856–63
- [29] Castellanos-Gomez A, Buscema M, Molenaar R, Singh V, Janssen L, van der Zant H S J and Steele G A 2014 Deterministic transfer of two-dimensional materials by all-dry viscoelastic stamping *2D Mater.* **1** 011002
- [30] Li H, Wu J, Huang X, Yin Z, Liu J, Zhang H and universal A 2014 Rapid method for clean transfer of nanostructures onto various substrates *ACS Nano* **8** 6563–70
- [31] Gurarslan A, Yu Y, Su L, Yu Y, Suarez F, Yao S, Zhu Y, Ozturk M, Zhang Y and Cao L 2014 Surface-energy-assisted perfect transfer of centimeter-scale monolayer and few-layer MoS<sub>2</sub> films onto arbitrary substrates *ACS Nano* **8** 11522–8
- [32] Feenstra R, Stroscio J A and Fein A 1987 Tunneling spectroscopy of the Si(111)2x1 surface *Surf. Sci.* **181** 295–306
- [33] Horcas I, Fernández R, Gómez-Rodríguez J M, Colchero J, Gómez-Herrero J and Baro A M 2007 WSXM: a software for scanning probe microscopy and a tool for nanotechnology *Rev. Sci. Instrum.* **78** 013705
- [34] Nečas D and Klapetek P 2012 Gwyddion: an open-source software for SPM data analysis *Cent. Eur. J. Phys.* **10** 181–8
- [35] Mak K F, Lee C, Hone J, Shan J and Heinz T F 2010 Atomically thin MoS<sub>2</sub>: a new direct-gap semiconductor *Phys. Rev. Lett.* **105** 136805
- [36] Liu C and Berg R W 2012 Determining the spectral resolution of a charge-coupled device (CCD) Raman instrument *Appl. Spectrosc.* **66** 1034–43
- [37] Kresse G and Hafner J 1993 *Ab initio* molecular dynamics for liquid metals *Phys. Rev. B* **47** 558–61
- [38] Kresse G and Furthmüller J 1996 Efficient iterative schemes for *ab initio* total-energy calculations using a plane-wave basis set *Phys. Rev. B* **54** 11169–86
- [39] Perdew J P, Burke K and Ernzerhof M 1996 Generalized gradient approximation made simple *Phys. Rev. Lett.* **77** 3865
- [40] Kresse G and Joubert D 1999 From ultrasoft pseudopotentials to the projector augmented-wave method *Phys. Rev. B* **59** 1758–75
- [41] Klimeš J, Bowler D R and Michaelides A 2011 van der Waals density functionals applied to solids *Phys. Rev. B* **83** 195131
- [42] Klimeš J, Bowler D R and Michaelides A 2010 Chemical accuracy for the van der Waals density functional *J. Phys.: Condens. Matter* **22** 022201
- [43] Kumar A and Ahluwalia P K 2012 Electronic structure of transition metal dichalcogenides monolayers 1H-MX<sub>2</sub> (M = Mo, W; X = S, Se, Te) from *ab-initio* theory: new direct band gap semiconductors *Eur. Phys. J. B* **85** 186
- [44] Johari P and Shenoy V B 2012 Tuning the electronic properties of semiconducting transition metal dichalcogenides by applying mechanical strains *ACS Nano* **6** 5449–56
- [45] Kadantsev E S and Hawrylak P 2012 Electronic structure of a single MoS<sub>2</sub> monolayer *Solid State Commun.* **152** 909–913
- [46] Noh J-Y, Kim H and Kim Y-S 2014 Stability and electronic structures of native defects in single-layer MoS<sub>2</sub> *Phys. Rev. B* **89** 205417
- [47] Komsa H-P and Krasheninnikov A V 2015 Native defects in bulk and monolayer MoS<sub>2</sub> from first principles *Phys. Rev. B* **91** 125304
- [48] Eckerlin P and Kandler H E 1971 *Group III: Condensed Matter (Landolt-Brönstein: Numerical Data and Functional Relationships in Science and Technology—New Series)* vol 6 (Berlin: Springer)
- [49] Pletikosić I, Kralj M, Sokčević D, Brako R, Lazić P and Pervan P 2010 Photoemission and density functional theory study of Ir(111); energy band gap mapping *J. Phys. Condens. Matter* **22** 135006
- [50] Chen W, Santos E J G, Zhu W, Kaxiras E and Zhang Z 2013 Tuning the electronic and chemical properties of monolayer MoS<sub>2</sub> adsorbed on transition metal substrates *Nano Lett.* **13** 509–14
- [51] Gong C, Colombo L, Wallace R M and Cho K 2014 The unusual mechanism of partial fermi level pinning at metal-MoS<sub>2</sub> interfaces *Nano Lett.* **14** 1714–20
- [52] Tersoff J and Hamann D 1985 Theory of the scanning tunneling microscope *Phys. Rev. B* **31** 805–13
- [53] Splendiani A, Sun L, Zhang Y, Li T, Kim J, Chim C Y, Galli G and Wang F 2010 Emerging photoluminescence in monolayer MoS<sub>2</sub> *Nano Lett.* **10** 1271–5
- [54] Mak K F, He K, Lee C, Lee G H, Hone J, Heinz T F and Shan J 2013 Tightly bound trions in monolayer MoS<sub>2</sub> *Nat. Mater.* **12** 207–11
- [55] Buscema M, Steele G A, van der Zant H S J and Castellanos-Gomez A 2014 Effect of the substrate on the raman and photoluminescence emission of single layer MoS<sub>2</sub> *Nano Res.* **7** 561–71
- [56] Yu Y, Yu Y, Xu C, Cai Y Q, Su L, Zhang Y, Zhang Y W, Gundogdu K and Cao L 2016 Engineering substrate interactions for high luminescence efficiency of transition-metal dichalcogenide monolayers *Adv. Funct. Mater.* **26** 4733–9
- [57] Liu Z *et al* 2014 Strain and structure heterogeneity in MoS<sub>2</sub> atomic layers grown by chemical vapour deposition *Nat. Commun.* **5** 5246
- [58] Conley H J, Wang B, Ziegler J I, Haglund R F, Pantelides S T and Bolotin K I 2013 Bandgap engineering of strained monolayer and bilayer MoS<sub>2</sub> *Nano Lett.* **13** 3626–30
- [59] Castellanos-Gomez A, Roldán R and Cappelluti E 2013 Local strain engineering in atomically thin MoS<sub>2</sub> *Nano Lett.* **13** 5361–6
- [60] Frisenda R, Drüppel M, Schmidt R, Michaelis de Vasconcellos S, Perez de Lara D, Bratschitsch R, Rohlfing M and Castellanos-Gomez A 2017 Biaxial strain tuning of the optical properties of single-layer transition metal dichalcogenides *Npj 2D Mater. Appl.* **1** 10
- [61] Wierzbowski J *et al* 2017 Direct exciton emission from atomically thin transition metal dichalcogenide heterostructures near the lifetime limit *Sci. Rep.* **7** 7–12
- [62] Plechinger G, Mann J, Preciado E, Barroso D, Nguyen A, Eroms J, Schüller C, Bartels L and Korn T 2014 A direct comparison of CVD-grown and exfoliated MoS<sub>2</sub> using optical spectroscopy *Semicond. Sci. Technol.* **29** 064008

- [63] Ajayi O A *et al* 2017 Approaching the intrinsic photoluminescence linewidth in transition metal dichalcogenide monolayers *2D Mater.* **4** 031011
- [64] Zhu B, Chen X and Cui X 2015 Exciton binding energy of monolayer WS<sub>2</sub> *Sci. Rep.* **5** 9218
- [65] Ross J S *et al* 2013 Electrical control of neutral and charged excitons in a monolayer semiconductor *Nat. Commun.* **4** 1474
- [66] Lu C-P, Li G, Mao J, Wang L-M and Andrei E Y 2014 Bandgap, mid-gap states, and gating effects in MoS<sub>2</sub> *Nano Lett.* **14** 4628–33
- [67] Castellanos-Gomez A, Quereda J, van der Meulen H P, Agrait N and Rubio-Bollinger G 2016 Spatially resolved optical absorption spectroscopy of single- and few-layer MoS<sub>2</sub> by hyperspectral imaging *Nanotechnology* **27** 115705
- [68] Kim J, Cote L J, Kim F and Huang J 2010 Visualizing graphene based sheets by fluorescence quenching microscopy *J. Am. Chem. Soc.* **132** 260–7
- [69] Gaudreau L, Tielrooij K J, Prawiroatmodjo G E D K, Osmond J, De Abajo F J G and Koppens F H L 2013 Universal distance-scaling of nonradiative energy transfer to graphene *Nano Lett.* **13** 2030–5
- [70] Sagar A, Kern K and Balasubramanian K 2010 Marker-free on-the-fly fabrication of graphene devices based on fluorescence quenching *Nanotechnology* **21** 015303
- [71] Chen Z, Berciaud S, Nuckolls C, Heinz T F and Brus L E 2010 Energy transfer from individual semiconductor nanocrystals to graphene *ACS Nano* **4** 2964–8
- [72] Rice C, Young R J, Zan R, Bangert U, Wolverson D, Georgiou T, Jalil R and Novoselov K S 2013 Raman-scattering measurements and first-principles calculations of strain-induced phonon shifts in monolayer MoS<sub>2</sub> *Phys. Rev. B* **87** 081307(R)
- [73] Chakraborty B, Bera A, Muthu D V S, Bhowmick S, Waghmare U V and Sood A K 2012 Symmetry-dependent phonon renormalization in monolayer MoS<sub>2</sub> transistor *Phys. Rev. B* **85** 161403(R)
- [74] Hui Y Y, Liu X, Jie W, Chan N Y, Hao J, Hsu Y-T, Li L-J, Guo W and Lau S P 2013 Exceptional tunability of band energy in a compressively strained trilayer MoS<sub>2</sub> sheet *ACS Nano* **7** 7126–31
- [75] Starodub E, Bostwick A, Moreschini L, Nie S, El Gabaly F, McCarty K F and Rotenberg E 2011 In-plane orientation effects on the electronic structure, stability, and raman scattering of monolayer graphene on Ir(111) *Phys. Rev. B* **83** 125428
- [76] Brako R, Šokčević D, Lazić P and Atodiresei N 2010 Graphene on the Ir(111) surface: from van der Waals to strong bonding *New J. Phys.* **12** 113016
- [77] Murata Y, Starodub E, Kappes B B, Ciobanu C V, Bartelt N C, McCarty K F and Kodambaka S 2010 Orientation-dependent work function of graphene on Pd(111) *Appl. Phys. Lett.* **97** 21–4
- [78] Zhou Q, Coh S, Cohen M L, Louie S G and Zettl A 2013 Imprint of transition metal D orbitals on a graphene Dirac cone *Phys. Rev. B* **88** 235431
- [79] N'Diaye A T, Coraux J, Plasa T N, Busse C and Michely T 2008 Structure of epitaxial graphene on Ir(111) *New J. Phys.* **10** 043033
- [80] Kang J, Li J, Li S-S, Xia J-B and Wang L-W 2013 Electronic structural moiré pattern effects on MoS<sub>2</sub>/MoSe<sub>2</sub> 2D heterostructures *Nano Lett.* **13** 5485–90
- [81] Jung J, Raoux A, Qiao Z and MacDonald A H 2014 *Ab initio* theory of moiré superlattice bands in layered two-dimensional materials *Phys. Rev. B* **89** 205414
- [82] Tong Q, Yu H, Zhu Q, Wang Y, Xu X and Ya W 2017 Topological mosaics in moiré superlattices of van der Waals heterobilayers *Nat. Phys.* **13** 356–62
- [83] Stolyarova E, Rim K T, Ryu S, Maultzsch J, Kim P, Brus L E, Heinz T F, Hybertsen M S and Flynn G W 2007 High-resolution scanning tunneling microscopy imaging of mesoscopic graphene sheets on an insulating surface *Proc. Natl. Acad. Sci.* **104** 9209–12
- [84] Ishigami M, Chen J, Cullen W, Fuhrer M and Williams E 2007 Atomic structure of graphene on SiO<sub>2</sub> *Nano Lett.* **7** 1643–8
- [85] Liu X, Balla I, Bergeron H and Hersam M C 2016 Point defects and grain boundaries in rotationally commensurate MoS<sub>2</sub> on epitaxial graphene *J. Phys. Chem. C* **120** 20798–805
- [86] Addou R, Colombo L and Wallace R M 2015 Surface defects on natural MoS<sub>2</sub> *ACS Appl. Mater. Interfaces* **7** 11921–9
- [87] Coraux J, N'Diaye A T, Busse C and Michely T 2008 Structural coherency of graphene on Ir(111) *Nano Lett.* **8** 565–70
- [88] Luican A, Li G and Andrei E Y 2009 Scanning tunneling microscopy and spectroscopy of graphene layers on graphite *Solid State Commun.* **149** 1151–6
- [89] Ondráček M, Pou P, Rozsival V, González C, Jelínek P and Pérez R 2011 Forces and currents in carbon nanostructures: are we imaging atoms? *Phys. Rev. Lett.* **106** 176101
- [90] Dedkov Y, Voloshina E and Fonin M 2015 Scanning probe microscopy and spectroscopy of graphene on metals *Phys. Status Solidi* **252** 451–68
- [91] Altibelli A, Joachim C and Sautet P 1996 Interpretation of STM images: the MoS<sub>2</sub> surface *Surf. Sci.* **367** 209–20
- [92] Magda G Z, Petö J, Dobrik G, Hwang C, Biró L P and Tapasztó L 2015 Exfoliation of large-area transition metal chalcogenide single layers *Sci. Rep.* **5** 14714
- [93] Kobayashi K and Yamauchi J 1995 Electronic structure and scanning-tunneling-microscopy image of molybdenum dichalcogenide surfaces *Phys. Rev. B* **51** 17085–95
- [94] Young P A 1968 Lattice parameter measurements on molybdenum disulphide *J. Phys. D: Appl. Phys.* **1** 936–8
- [95] Tongay S *et al* 2013 Defects activated photoluminescence in two-dimensional semiconductors: interplay between bound, charged, and free excitons *Sci. Rep.* **3** 2657
- [96] Hill H M, Rigosi A F, Roquelet C, Chernikov A, Berkelbach T C, Reichman D R, Hybertsen M S, Brus L E and Heinz T F 2015 Observation of excitonic rydberg states in monolayer MoS<sub>2</sub> and WS<sub>2</sub> by photoluminescence excitation spectroscopy *Nano Lett.* **15** 2992–7
- [97] Zhang C, Johnson A, Hsu C-L, Li L-J and Shih C-K 2014 Direct imaging of band profile in single layer MoS<sub>2</sub> on graphite: quasiparticle energy gap, metallic edge states, and edge band bending *Nano Lett.* **14** 2443–7
- [98] Tersoff J and Hamann D 1983 Theory and application for the scanning tunneling microscope *Phys. Rev. Lett.* **50** 1998–2001
- [99] Liu L, Chen Z, Wang L, Polyakova E, Taniguchi T, Watanabe K, Hone J, Flynn G W and Brus L E 2013 Slow gold adatom diffusion on graphene: effect of silicon dioxide and hexagonal boron nitride substrates *J. Phys. Chem. B* **117** 4305–12
- [100] Zhou W, Zou X, Najmaei S, Liu Z, Shi Y, Kong J, Lou J, Ajayan P M, Yakobson B I and Idrobo J-C 2013 Intrinsic structural defects in monolayer molybdenum disulfide *Nano Lett.* **13** 2615–22
- [101] Qiu H *et al* 2013 Hopping transport through defect-induced localized states in molybdenum disulphide *Nat. Commun.* **4** 2642
- [102] González C, Biel B and Dappe Y J 2016 Theoretical characterisation of point defects on a MoS<sub>2</sub> monolayer by scanning tunnelling microscopy *Nanotechnology* **27** 105702